Title

Atomic-Scale Imaging Reveals Polar–π Interactions in Two-Dimensional Molecular Superlattices

Journal

Journal of the American Chemical Society, 148(13)

ISSN

0002-7863

Authors

Lee, Yen Jea

Butterfoss, Glenn L

Luo, Xubo

et al.

Publication Date

2026-04-08

DOI

10.1021/jacs.5c19396

Atomic-Scale Imaging Reveals Polar-π Interactions in Two-Dimensional Molecular Superlattices

Yen Jea Lee [a], Glenn L. Butterfoss [b], Xubo Luo [c], David Prendergast [c], Nitash P. Balsara [a, d], Ronald N. Zuckermann [c*], Brooks A. Abel [a, e*], and Xi Jiang [a*]

[a] Materials Sciences Division, Lawrence Berkeley National Laboratory, Berkeley, California, 94720, United States.

[b] Center for Genomics and Systems Biology, New York University, New York City, New York, 10003, United States.

[c] Molecular Foundry, Lawrence Berkeley National Laboratory, Berkeley, California, 94720, United States.

[d] Department of Chemical and Biomolecular Engineering, University of California, Berkeley, California, 94720, United States.

[e] Department of Chemistry, University of California, Berkeley, California, 94720, United States.

*Corresponding authors:

Ronald N. Zuckermann, Ph.D. (e-mail: rnzuckermann@lbl.gov)

Brooks A. Abel, Prof. (e-mail: brooks.abel@berkeley.edu)

Xi Jiang, Ph. D. (e-mail: xijiang@lbl.gov)

ABSTRACT

Controlling co-assembly of synthetic oligomers into binary superlattices at the atomic level is challenging. We report a strategy for programming polar-π interactions in oligomeric peptoids, a class of sequence-defined peptidomimetics, facilitating the formation of homogeneous two-dimensional (2D) superlattices. *N*-2-phenylethyl and *N*-(2-perfluorophenyl)ethyl side chains, similar in size, but with contrasting electrostatic characteristics, were introduced at defined sequence positions to generate favorable dipolar aromatic interactions. The resulting nanosheets exhibit different crystal motifs depending on the side chain interactions: systems containing only one type of aromatic side chain form a parallel V-shaped motif driven by π-π interactions, whereas a combination of both types of aromatic side chains, either within one backbone or through the co-assembly of two distinct peptoids, adopt an antiparallel V-shaped superlattice with higher thermal stability, driven by polar-π interactions. Cryogenic transmission electron microscopy directly resolved the packing arrangement of perfluorophenyl and phenyl rings in individual nanosheet superlattices, confirming that intermolecular polar-π interaction dominates the superlattice motifs and increases lattice stability. Molecular dynamics simulations and density functional theory calculations further substantiate the energetic favorability of polar-π interactions over π-π interactions, rationalizing the formation of homogeneous superlattices with enhanced thermal stability. Our discoveries establish a design principle for binary co-assembly using sequence-defined oligomers, which enables control over unit cell geometry, lattice stability, and molecular registration through aromatic side chain polarization and sequence control. This

ability to program atomic-scale binary superlattices opens new avenues for designing functional 2D soft materials.

INTRODUCTION

Hierarchical nanostructures are a cornerstone of materials science,[1, 2] with applications in microelectronics,[3, 4] energy storage,[5, 6] catalysis,[7, 8] and quantum sensing.[9, 10] To expand the functional scope of self-assembled nanostructures, strategies based on conjugating chemically distinct functionalities onto a single lattice-forming building block have been widely employed.[11-13] However, in such approaches, these functionalities necessarily share the same crystallographic unit and therefore become statistically distributed within the lattice, which intrinsically limits precise molecular-level control over their relative positioning and interactions. In contrast, co-assembly of distinct building blocks into ordered superlattices comprising two or more components can provide an effective route to chemical diversity and multifunctionality with high structural precision.[14]

The creation of robust superlattice architectures often relies on non-covalent interactions such as hydrogen bonding,[15] aromatic interactions,[16-18] ligand-acceptor binding,[19, 20] and chirality.[21] These approaches can bring together biological molecules (e.g., peptides,[22, 23] or proteins[24, 25]), synthetic polymers,[15, 26-28] and chemically-modified entities (e.g. functionalized nanoparticles[29] or two-dimensional (2D) material heterostructures[30]) to create multidimensional superlattice architectures. Despite these advances, the straightforward fabrication of molecular superlattices without phase separation, conformational change, or atomic-scale lattice heterogeneity remains elusive, particularly in synthetic soft materials. The challenge comes

from narcissistic self-sorting,[31, 32] where identical molecules tend to assemble into their own lattice instead of forming a superlattice composed of different molecules, driven by factors such as molecular geometry,[33] steric effects,[34] and chirality.[35] Furthermore, phase separation serves as a fundamental physical limitation that hinders the formation of sub-nanometer-level ordered lattices in polymer blends and self-assembled materials,[36] and represents a key challenge that must be addressed to advance the charge separation and transport in polymer-based organic electronics.[37]

Amphiphilic diblock peptoids, poly(*N*-substituted glycines),[38] are sequence-defined peptidomimetics. They self-assemble in solution into a variety of crystalline nanostructures with a range of functional properties.[39-44] Previous studies on 2D peptoid nanosheets have primarily focused on the formation of crystal lattices from single-component systems.[42, 45-47] However, constructing predictable unit cells with molecular-level precision and regulating interactions between distinct oligomeric peptoids to form homogeneous binary superlattices remain major challenges. Achieving molecular-level control over co-assembly of distinct peptoids has been elusive due to the lack of understanding of the underlying driving forces that govern the conformations and spatial arrangement of co-assembled peptoids. [13, 41, 43, 48]

In this work, we aim to design 2D molecular superlattices that consist of two different diblock peptoid oligomers in a single nanosheet. Experimentally demonstrating the coexistence of two different molecules in such superlattices requires engineered structural diversity within the same nanosheet to enable atomic-scale structural characterization in real space.[48] Cryogenic transmission electron microscopy (cryo-TEM) has been employed to resolve molecular arrangement and non-covalent interactions, such as π-π interactions, in hierarchical structures formed by peptides,[49, 50] supramolecular systems,[51, 52] cation-π interactions in proteins,[53, 54] as well as the single-component crystal motifs formed by diblock peptoids.[42, 55] The atomic-scale

imaging of 2D superlattices in this study provides direct evidence and insights into their underlying design principles.

The 2D nanosheets comprised of these diblock peptoids adopt a corona architecture, with hydrophobic blocks forming a well-ordered crystalline core, and hydrophilic blocks exposed to water and stabilizing the sheet, as shown in Figure 1A.[42, 45] The molecular packing of oligomeric peptoids bearing *N*-2-phenylethylglycine monomers in a unit cell was revealed previously (Figure S1); the assembly is driven by π-π stacking of the side chains and CH•••O=C hydrogen bonding between glycine backbones in hydrophobic blocks.[42] The lattice shown in Figure 1A exhibits two characteristic spacings: the (100) spacing along the *a*-axis, which corresponds to the backbone-to-backbone distance between adjacent molecules in a row, and the (002) spacing along the *c*-axis, which corresponds to the distance between the centers of molecules in neighboring peptoid rows.

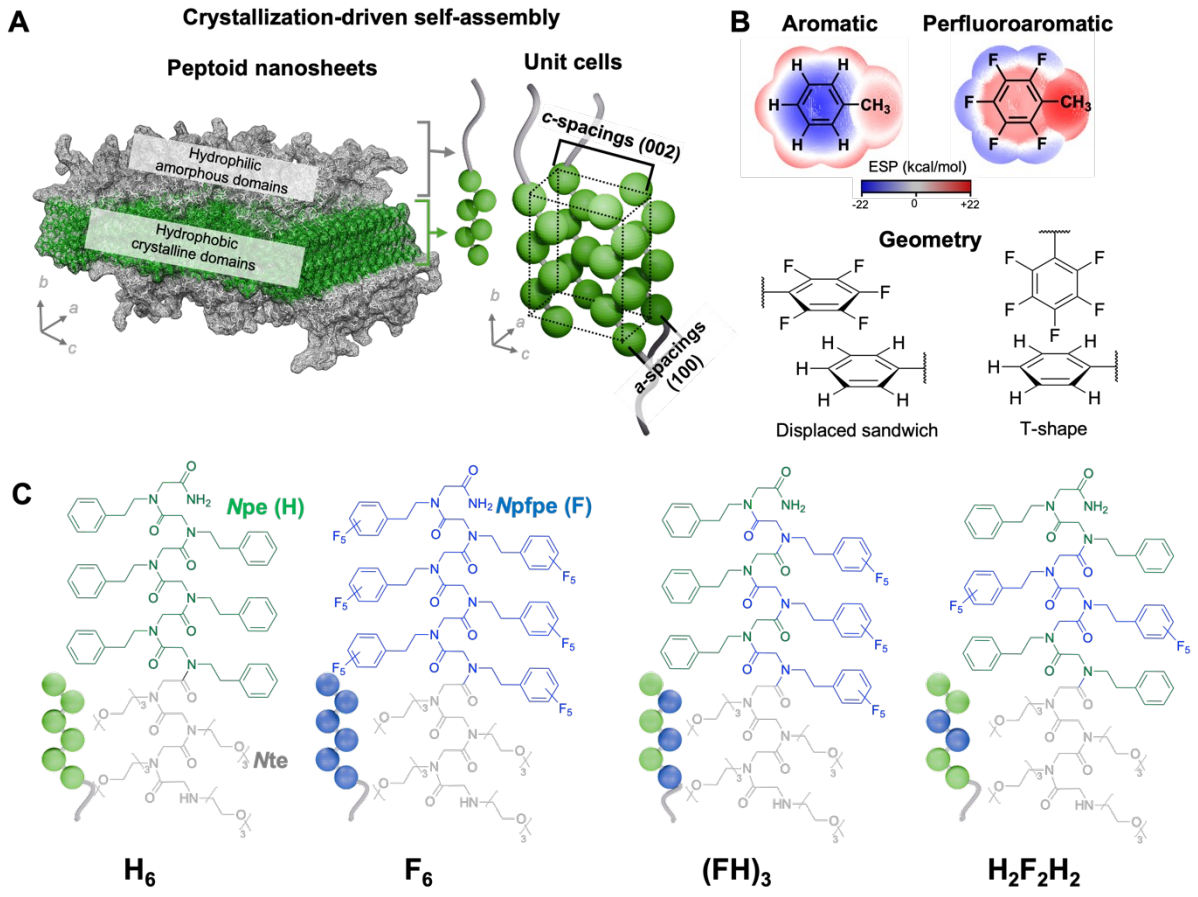

Figure 1. (A) Schematic representation of peptoid nanosheets and unit cell motifs. (B) The electrostatic potential (ESP) surface calculated for geometry optimized toluene and pentafluorotoluene at the B3LYP/6–311G(d,p) level of theory (see SI for detailed DFT calculation procedures), presenting the opposite electrostatic properties on the surface of aromatic and perfluoroaromatic rings, and the geometries of polar-π interactions between them.[56, 57] (C) Chemical structures of diblock peptoids synthesized. The location of phenylethyl (*N*pe) and perfluorophenylethyl(*N*pfpe) side chains are represented by green and blue spheres, respectively, in the hydrophobic blocks. The hydrophilic blocks are represented by tails for simplicity.

Based on the established lattice structure formed by diblock peptoids,[42] we hypothesized that engineering the location of different aromatic side chains with atomic-scale accuracy could enable polar-π interactions, a unique form of π-π interaction wherein an electron-rich aromatic ring preferentially aligns with an electron-deficient aromatic ring as a pair with various geometries (Figure 1B),[58, 59] which are widely exploited to drive co-assembly[60, 61] and charge-transfer pathways in soft matter.[62, 63]

Polar-π interactions play a crucial role in directing molecular packing and assembly in complex systems.[64-66] Representative aromatics pairs such as benzene and hexafluorobenzene are known to form 1:1 displaced sandwich complexes stabilized by polar-π interactions with a low melting temperature (~23.7 °C).[67, 68] Subsequent studies on benzene-hexafluorobenzene and their derivatives have identified three characteristic geometries, such as displaced sandwich, sandwich, and T-shaped (edge-to-center) one, with stabilization energies decreasing in this order (bottom panel, Figure 1B).[57] While alternate stacking between benzene and hexafluorobenzene is a well-established synthon in small-molecule crystallography,[66, 69] implementing this interaction within oligomeric scaffolds presents fundamentally different challenges. The rotational freedom of the chains and complex intramolecular interactions among the backbone and side chains give rise to a broad conformational ensemble for oligomeric chains in solution. Precisely controlling these conformational dynamics to achieve long-range order with minimal defects, and to understand this process at the molecular level, remains a significant challenge.

Here, we aim to explore whether the highly specific polar-π interactions could be introduced into the sequence-defined oligomeric systems. The electrostatic potential (ESP) surfaces of toluene and perfluorotoluene were calculated to represent the aromatic and perfluoroaromatic rings, although a cocrystal structure of these two has not been reported yet

(top panel, Figure 1B). The calculations revealed that the two molecules exhibit contrasting electrostatic potentials, leading us to anticipate that polar-π interactions could arise from the pairing of aromatic and perfluoroaromatic rings. Thus, we introduced perfluorophenylethyl and phenyl side chains into the hydrophobic blocks of amphiphilic diblock peptoids at various sequence positions (Figure 1C). We hypothesized that the 2D peptoid lattice would not be sterically disrupted by perfluorophenyl ring substitution, based on the similar ring diameters of toluene (4.9 Å) and the nearly isosteric perfluorotoluene (5.4 Å) (Figure 1B). By arranging perfluorophenyl and phenyl groups along a linear peptoid sequence, we enabled the formation of intermolecular polar-π interactions upon chain self-association.

Using this design, we aimed to achieve a 1:1 pairing of these moieties within the lattice, using two strategies: segregating them within a single chain or by mixing two chains. Through subtle variation of the peptoid composition and sequence, the competing driving forces of polar-π versus conventional π-π interactions were investigated. This series of nanosheet-forming molecules provide a platform to fabricate molecular superlattices with atomic-scale precision, which remains a major challenge in synthetic soft materials.[70-73]

This work addressed three fundamental challenges in understanding the role of polar-π interactions in governing co-assembly behavior leading to regular lattices or superlattices: First, we designed molecules that can facilitate polar-π interactions to form lattices with enhanced stability. Second, we directly visualized the molecular packing arrangement at atomic resolution using cryo-TEM, which clearly elucidated molecular configurations within lattices. Third, the atomic-scale imaging of lattices provided strong structural constraints for modeling the effect of polar-π interactions in the formed lattices. By integrating the experimentally determined crystal motifs with molecular dynamics (MD) and density functional theory (DFT) calculations, we obtained molecular-level insight into the chain

conformations within each lattice and how the geometry of polar-π interactions directs molecular packing in different crystal motifs with different structural stability. Our findings provide a new approach to fabricating molecular superlattices, which sheds light on implications for the design of hierarchical nanostructures with tailored properties at atomic-scale precision.

RESULTS AND DISCUSSION

Molecular Design

We designed and synthesized a series of diblock peptoids, each composed of a crystalline hexameric hydrophobic segment made from either *N*-2-phenylethyl glycine (*N*pe, H) or *N*-2-perfluorophenylethyl glycine (*N*pfpe, F), with an amorphous hydrophilic segment consisting of four *N*-2-(2-(2-methoxyethoxy))ethylglycine (*N*te) residues (Figure 1C). While highly fluorinated aliphatic monomers have been incorporated in peptoid synthesis, perfluoroaromatic monomers like *N*pfpe have not been reported in designing peptoids. The primary amine for this monomer, 2-perfluorophenylethyl amine, was synthesized in three steps from perfluorophenyl methanol using previously reported methods (Section 2.1 in the Supporting Information and Figure S2).[74, 75] We then designed a set of *N*pfpe-containing peptoids based on the established packing model of *N*te$_4$-*N*pe$_6$ (abbreviated as H$_6$) in nanosheets (Figure 1C).[42] The ratio and sequence pattern of *N*pfpe monomers within the hydrophobic block were varied to investigate how the perfluorophenyl-phenyl interaction affects the formation of the unit cell in the resulting peptoid nanostructures. *N*te$_4$-*N*pfpe$_6$, abbreviated as F$_6$, has a hydrophobic block that consists entirely of perfluorophenylethyl side chains. *N*te$_4$-(*N*pfpe*N*pe)$_3$, abbreviated as (FH)$_3$, incorporates a regularly alternating pattern of *N*pe and *N*pfpe monomers, while the sequence *N*te$_4$-*N*pe$_2$*N*pfpe$_2$*N*pe$_2$ (H$_2$F$_2$H$_2$) features a distinct blocked arrangement within the hydrophobic domain. All diblock peptoids were purified using reverse-phase high-performance liquid chromatography (RP-HPLC) to achieve purities exceeding 95% (Figures S3 and S4).

Homogeneous regular lattices

Peptoid self-assembly was conducted using the approach reported by Xuan et al (Supporting Information section 2.3).[42] Peptoids were dissolved in a 1:1 (v/v) THF/H_2O mixture, and the THF was allowed to evaporate gradually over 14 days at 4 ˚C. Five nanosheet samples were prepared: the homogeneous diblock peptoids, H_6, F_6, $(FH)_3$, $H_2F_2H_2$, and a 1 : 1 molar mixture of H_6 and F_6. The first four peptoid sequences were designed to undergo homogenous assembly into regular lattices, whereas the mixed H_6+F_6 molecules were designed to co-assemble into a binary superlattice.

We began with the previously reported H_6 diblock peptoid,[42] which produced well-defined rectangular micron-scale nanosheets, (Figure S5A), and served as the reference structure in this work. In contrast, no ordered nanostructures were observed by SEM for F_6, $(FH)_3$, $H_2F_2H_2$, after the initial 14 days evaporation (Figure S6). These solutions were then sealed and left at 4 °C for an additional seven days (21 days total). After this extended incubation, nanosheets appeared for F_6 and for $(FH)_3$, (Figure S7) whereas $H_2F_2H_2$ did not form 2D nanosheet structures (Figure S8). This result is attributed to a sequence-dependent effect on the kinetics of nucleation and formation of peptoid nanosheets. Although $H_2F_2H_2$ exhibited an intermediate hydrophobicity between H_6 and F_6, as indicated by ultra-performance liquid chromatography (UPLC) retention times (t_R = 5.0 min for H_6, t_R = 5.5 min for $H_2F_2H_2$, and t_R = 6.0 min for F_6, Figure S3), it did not self-assemble into nanosheets, suggesting that hydrophobicity alone is insufficient to promote nanosheet formation and unit cell organization into the thin 2D lattices, and instead points to a minimum requirement of sequence patterning to nucleate a 2D lattice in solution. While both F_6 and $(FH)_3$ required additional incubation time to

assemble, a 1:1 molar ratio of H_6 and F_6 co-assembled into nanosheets without additional incubation time.

Nanosheets obtained from H_6, F_6, $(FH)_3$, and the 1:1 H_6+F_6 mixture were imaged by AFM (Figures 2A to 2D). Height analysis indicated a uniform thickness between 3 and 4 nm for all four nanosheets (Table S1, and Figure S11 and S12), consistent with the monolayer architecture depicted in Figure 1A. It is noteworthy that their micron-scale morphologies varied significantly depending on the monomer sequence. H_6 sheets appear as rectangular ribbons with sharp, well-defined edges where F_6 sheets are elongated, small oval-shaped sheets bearing rugged sides and tapered ends. Both the $(FH)_3$ self-assembled and the H_6+F_6 co-assembled nanosheets produced rectangular ribbons with highly defined sides and tapered ends. The lattice orientations were identified by indexing the reflections in the power spectra of cryo-TEM images obtained from a H_6 sheet (Figure S9). The long and short dimensions of ribbons are attributed to *a*- and *c*-axes in the lattice, respectively (Figures 1A and 2A). We posit that the different anisotropic growth rates along the crystallographic *a*- and *c*-axes may arise from the difference between π-π and polar-π interactions.

Powder X-ray diffractions (PXRD) of the dried nanosheets formed from H_6, F_6, $(FH)_3$, and the 1 : 1 H_6+F_6 mixture are shown in Figures 2E–H. All samples showed sharp diffraction peaks, confirming high crystalline order. The reference H_6 nanosheets exhibited four major reflections at d ≈ 16.0 Å (002), 5.3 Å (006), 4.5 Å (100) and 4.2 Å (101), reproducing previously reported lattice parameters and serving as a benchmark for the other samples.[42] F_6 nanosheets were also crystalline, but the (002) reflection is broadened and weak; its position, inferred from the harmonic (006) at 5.8 Å, corresponds to a spacing of ≈ 17.4 Å, indicating a modest expansion of the inter-row distance and reduced long-range order along the *c*-axis,

consistent with the less well-defined sheet edges. Both $(FH)_3$ nanosheets and the H_6+F_6 co-assembled nanosheets exhibit a dominant (002) peak near 17.2 Å and, uniquely, an additional (100) reflection at 8.8 Å and 9.0 Å, respectively, which are absent in the H_6 and F_6 nanosheets. This extra peak reflects a superlattice periodicity along the *a*-axis. Consequently, all four nanosheet systems share a common basic lattice framework; they differ primarily in the *c*-axis spacing (the inter-row distance), and the presence of a superlattice peak with a nearly doubled *a*-axis spacing (from ≈ 4.5 Å to ≈ 9 Å) as summarized in Figure 2I.

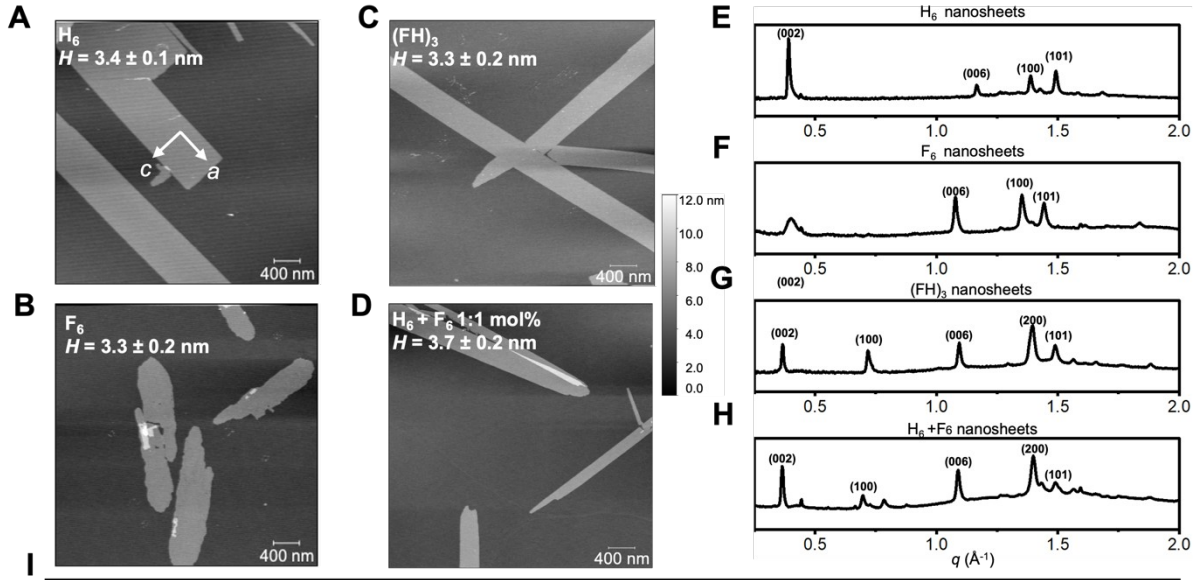

I

Nanosheets	Packing	Spacings in PXRD (Å) [a]		Spacings in TEM (Å) [b]		T_m (°C) [c]	ΔH (kcal/mol) [c]
		a /superlattice	*c*	*a* /superlattice	*c*		
H_6	Parallel	4.5 (100)	16.0 (002)	4.5 (100)	16.2 (002)	87	20.3
F_6	Parallel	4.6 (100)	17.4 (002)	4.7 (100)	17.5 (002)	53	13.4
$(FH)_3$	Anti-parallel	4.5 (200) /8.8 (100)	17.2 (002)	4.5 (200) /9.1 (100)	17.4 (002)	72	14.6
H_6+F_6 [d]	Anti-parallel	4.5 (200) /9.0 (100)	17.2 (002)	4.5 (200) /9.1 (100)	17.5 (002)	95	>22.1

Figure 2. AFM (A–D) and PXRD (E–H) analysis. AFM images and height measurements of peptoid nanosheets: (A) H_6 (14 days evaporation), (B) F_6 (14 days evaporation and 7 days more incubation), (C) $(FH)_3$ (14 days evaporation and 7 days more incubation), and (D) H_6+F_6 (1:1 molar ratio) (14 days evaporation). *H* indicates the average nanosheet thickness measured with

z-height of AFM images (Table S1). PXRD spectra of dried nanosheets: (E) H_6, (F) F_6, (G) $(FH)_3$, and (H) H_6+F_6 (1:1 molar ratio). (I) Summary of structural parameters observed with peptoid nanosheets. [a] measured with PXRD patterns by fitting each peak with gaussian curves. [b] measured with FFT images from cryo-TEM images (Figure 3A–D). [c] Melting temperatures and enthalpy were measured using solution DSC (nanoDSC) (Figure S10). [d] 1:1 molar ratio.

The melting transition temperatures (T_m) of the solvated nanosheets, which reflect the relative stabilities, were measured using solution-state differential scanning calorimetry (DSC) in water (Figures 2I and S10). Co-assembled H_6+F_6 (1:1) nanosheets exhibited the highest T_m at 95 ˚C, followed by the reference H_6 nanosheets at 87 ˚C, and $(FH)_3$ nanosheets at 72 ˚C, while the F_6 nanosheets exhibited the lowest T_m at 53 ˚C. The enthalpy of melting (ΔH) follows the same trend as the melting temperatures (Figure 2I), suggesting that the variation in thermal stability among the different nanosheets is influenced by the type of interactions (polar-π or π-π) formed by molecules with different side chains in the lattices. The computed nonbonded energies from MD simulations are listed in Table S2 for reference.

Molecular lattice structures revealed by Cryo-TEM

Cryo-TEM imaging and the corresponding power spectrum in Figure 3A shows the lattice structure of the previously reported nanosheets formed by H_6.[33] The lattice dimensions are indicated by blue arrows: $a = 4.5$ Å (100) and $c = 32.2$ Å (001). The brightest features are seen as spots at the center of each molecule and correspond to the projected view of the glycine backbones that are oriented vertically within the nanosheet plane, while the extended arms emanating from these bright spots in a parallel V-shaped packing motif represent the 2-phenylethyl side chains. This structure serves as the reference for the comparisons in the following discussion. Black arrows in the image indicate a cross-section through the side

chains; the resulting 1-D intensity profile shows a uniform intensity across each molecule as expected (middle panel, Figure 3A), and the power spectrum of the image shows reflections from lattices (bottom panel, Figure 3A). The schematic arrangement of H_6 molecules in the nanosheets is shown in Figure 3E.

Cryo-TEM imaging of nanosheets formed by F_6 revealed similar features to those formed with H_6, as evidenced by the identical parallel V-shaped packing motif and the uniform intensity of side chains as indicated by their cross-sectional intensity profile (Figure 3B). However, the unit cell dimensions indicated by yellow arrows, a = 4.7 Å (100) and c =34.8 Å (001), are different as shown in the cryo-TEM image and power spectrum (bottom, Figure 3B). The increase of spacing along the *c*-axis is attributed to the larger space occupied by fluorine substituents at the *para* position as compared to hydrogen atoms. The model of homo-assembled lattice formed by the F_6 molecules with featured lattice spacings is depicted in Figure 3F. We posit that the molecular arrangement is nearly identical to the lattice formed by H_6 molecules.

The lattice structure formed by $(FH)_3$ molecules is different from the lattices formed by H_6 and F_6, as shown in Figure 3C (top panel). Instead of the parallel V-shaped motif, the alternating arrangement of side chains with different lengths can be observed along the *a*-axis in an antiparallel V-shaped motif. The intensity profile shown in the middle panel (black arrow on top panel, Figure 3C) exhibits a periodic intensity in contrast. Peaks of higher intensity correspond to the perfluorophenylethyl side chains; five fluorine atoms with higher atomic number relative to hydrogen atoms enhances the contrast in the image (Figure S14A). We therefore conclude that the longer and brighter arms in the image represent perfluorophenylethyl groups, whereas the shorter arms correspond to phenylethyl groups.

Importantly, in the antiparallel V-shaped packing motif, the shorter phenylethyl side chains are consistently oriented towards the neighboring perfluorophenylethyl side chains (indicated by green and blue arrows), leading to a tip-to-tip packing geometry between perfluorophenylethyl and phenylethyl side chains along the *c*-axis. Along the *a*-axis, the perfluorophenylethyl and phenylethyl side chains are alternatively packed through the polar-π interactions. The unit cell dimensions changed to $a = 9$ Å (100) and $c = 34.8$ Å (001) due to the presence of the alternating side chains. The power spectrum revealed new rows of reflections at 9 Å due to the presence of the alternating side chains, which doubles the lattice spacing along the *a*-axis while the *c*-axis spacing remains the same. The molecular arrangement of molecules is shown in the model in Figure 3G.

Direct molecular imaging by cryo-TEM, without extrinsic labeling, revealed the π-π or polar-π driven packing of phenyl and perfluorophenyl peptoids within the 2D lattice. For symmetric side chains, such as all phenylethyl (H_6) or all perfluorophenylethyl (F_6), where π-π interactions predominate, a parallel V-shaped packing motif was observed. In contrast, the $(FH)_3$ nanosheets, which contain both phenylethyl and perfluorophenylethyl side chains, adopt an antiparallel V-shaped packing motif, where perfluorophenyl side chains are oriented tip-to-tip with phenyl side chains along the *c*-axis, with alternating packing along the *a*-axis driven by polar-π interactions. The dominance of polar-π interactions in the $(FH)_3$ lattice raises a key question: what lattice structure will form from a 1:1 mixture of H_6 and F_6? The lattice parameters from X-ray diffraction and the increased melting temperature ($T_m = 95$ °C) indicate that the H_6+F_6 co-assembly forms a highly stable crystalline structure. The increased thermal stability is likely due to the polar-π interactions shown to be abundant by cryo-TEM.

The lattice structure of the H_6+F_6 co-assembly is shown in Figure 3D. In contrast to the crystal motifs observed for the single component lattices from self-assembled H_6 or F_6, the co-assembled lattice exhibits an antiparallel V-shaped packing motif with an alternating arrangement of two molecules within a row in the *a*-direction, that can be readily distinguished by their distinct side-chain length and intensity (indicated by the cross-sectional intensity profile). The shorter, lower-intensity arms correspond to the projection of phenyl rings, whereas the longer, higher-intensity protrusions correspond to perfluorophenyl rings. A simulated electrostatic-potential map reproduces this contrast, confirming that the observed features arise from the two different side chains (Figure S14B). To our best knowledge, no previous electron microscopy studies have resolved perfluorophenyl from phenyl rings by direct imaging in position space within crystalline synthetic soft materials.

In the H_6+F_6 crystal lattice, the molecules adopt an antiparallel V-shaped packing motif: alternating phenyl and perfluorophenyl side chains engage in polar-π interactions along the *a*-axis and in a tip-to-tip geometry across adjacent rows along the *c* direction to form a superlattice. The power spectrum shows a (002) reflection at 17.4 Å, in agreement with the X-ray diffraction pattern (bottom panel, Figure 3D). Additional reflections at 9 Å (100) indicate that the *a*-axis unit-cell dimension is doubled relative to the H_6 or F_6 lattices. By comparison, the $(FH)_3$ lattice also shows a 9 Å (100) spacing in the power spectrum (Figure 3C) but retains a regular lattice because the different side chains are incorporated within a single molecule. The schematic model in Figure 3H illustrates the alternating H_6 and F_6 molecules within the superlattice. After evaluating more than twenty nanosheets, all sheets were determined to have identical lattice spacings, demonstrating homogeneous co-assembly at a 1 : 1 molar ratio (more examples are shown in Figure S15). We posit that the stronger polar-π interactions present in co-assembled H_6+F_6 nanosheets drive the formation of a homogeneous superlattice and prevent

the formation of self-assembled regular lattices that would result from the weaker π-π interaction of H_6 and F_6 individually.

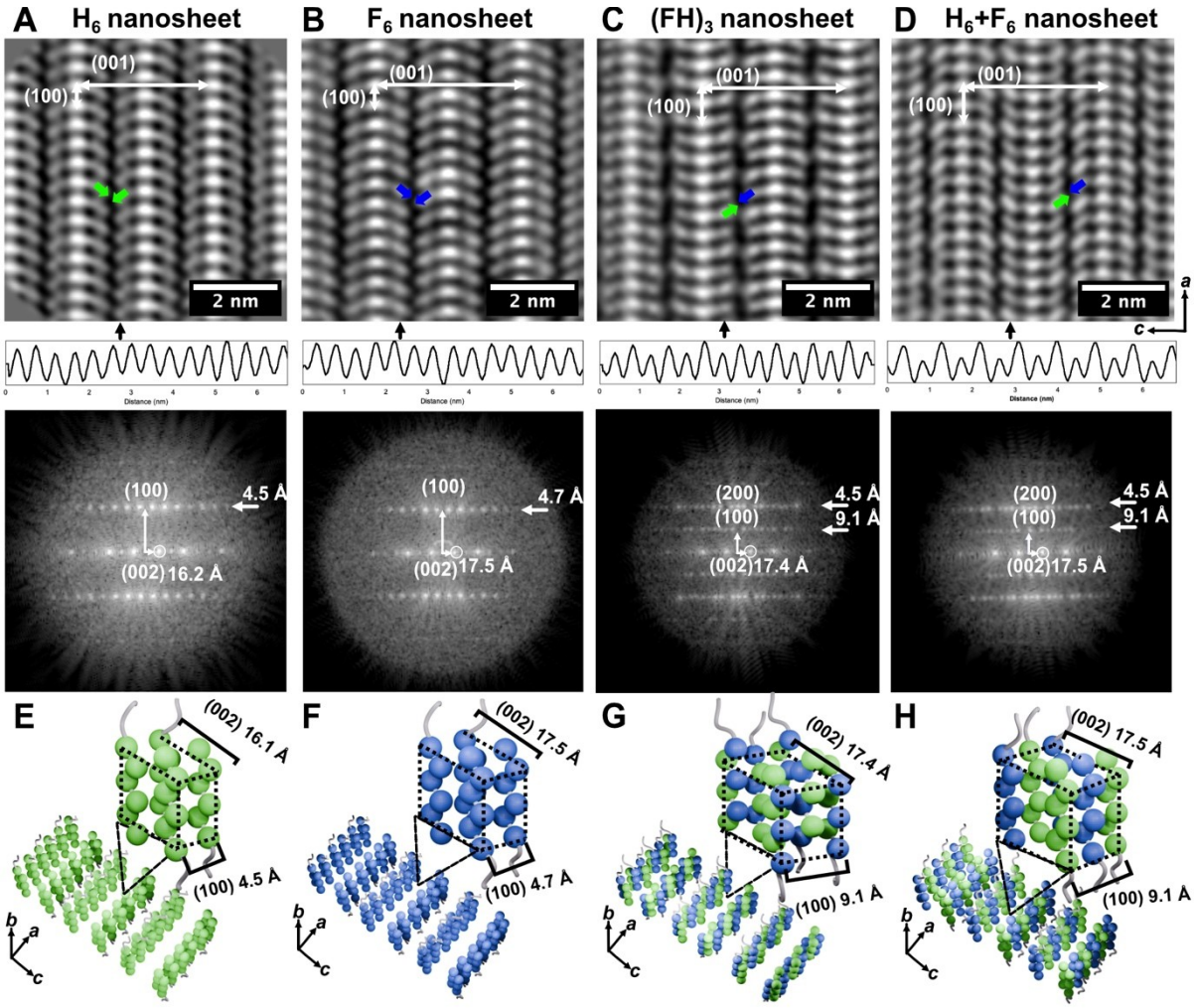

Figure 3. Cryo-TEM analysis of peptoid nanosheets. Averaged cryo-TEM images of (A) H_6 nanosheets, (B) F_6 nanosheets, (C) $(FH)_3$ nanosheets, and (D) co-assembled H_6+F_6 nanosheets (1:1 molar ratio). White arrows in the cryo-TEM images (top panels) indicate *a*-spacing (100) and *c*-spacing (002). The brightness profiles (middle panels) correspond to intensity traces taken along the black arrows in the cryo-TEM images. Green thick arrows denote the orientation of phenylethyl side chains, and blue thick arrows indicate the orientation of perfluorophenylethyl side chains. Corresponding power spectra of the averaged cryo-TEM images respectively are shown in the bottom panels. (E–H) Schematic models of each nanosheet derived from cryo-TEM images (A to D). Green spheres represent *N*spe monomers, and blue spheres represent *N*pfpe monomers. The parallel V-shaped motif in A and B possesses

plane symmetry *cm*, which imposes systematic absences in the Fourier space when $h+k$ is odd.[42]; consequently the (100) and (001) reflections are not visible in power spectrum (indicated by arrows). The antiparallel V-shaped motif in C and D exhibits the different plane symmetry, *pmg*, which leads to the symmetry forbidden of reflections in Fourier space when k=0, h =odd. Thus, the (200) at 4.5 Å and (002) at 17.4 Å are visible as indicated by the dashed arrows.[47] Raw micrographs can be found in Figure S13.

The role of polar-π interactions in lattices

Atomistic models were constructed based on the lattices observed in PXRD patterns and cryo-TEM images. Here, we adopted an all-*cis* conformation, given that the lattice parameters are in good agreement with those reported in the literature.[45, 76-78]

All-*cis* conformations form enantiomeric conformers because the linear backbone arises from alternating dihedral angles of opposite sign, and inversion of these dihedrals generates a mirror-related all-*cis* structure.[42, 79, 80] None of the experimental evidence, such as PXRD and cryo-TEM analysis, suggests the coexistence of two enantiomers in the same lattice along with *a*-axis although we expect both enantiomers to be present in equal amounts in different individual nanosheets. However, confirming this is still an open question and beyond the resolution of cryo-TEM 2D imaging. We thus posit that molecules preferentially adopt a single enantiomer for H_6 and F_6 (Figure 4A), as mixing two enantiomers in the same lattice would introduce an offset between neighboring chains (to accommodate the favorable alignment of backbones with each other in the *a*-axis), which destabilizes the lattice due to a loss of aromatic interactions. Accordingly, we modeled homogeneous H_6 and F_6, and 1:1 H_6+F_6 nanosheets using only a single enantiomer (Figures S16A, S17A and S19A).

By contrast, the crystal motif formed by $(FH)_3$ molecules (Figure 3C) shows the alternating packing of side chains within a row along with *a*-axis, where phenylethyl and perfluorophenylethyl side chains face one another in adjacent molecules along the *a*-axis to form polar-π interactions. We, therefore, propose that $(FH)_3$ molecules need to have an alternating backbone chirality (two enantiomers) within each row of the lattice as shown in Figure 4D. This molecular packing, which maximizes backbone-backbone interactions and π-π interactions, enabled us to construct an initial MD model (Figure S18A) that closely reflects the perfluorophenyl-phenyl face-to-face stacking observed in cryo-TEM images (Figure 3C). In

models of $(FH)_3$ nanosheets made from molecules of a single enantiomer within one row, they prefer to assemble with homogeneous facial packing between aromatic side chains, where all phenylethyl side chains pack on one side and fluorophenyl ethyl side chains pack on the other side of the backbones, facilitating π-π interactions instead of polar-π interactions. Detailed MD modeling is provided in the Supporting Information (Supplementary Note 1). Our model for $(FH)_3$ nanosheets implies that, even in nanosheets composed of a single type of peptoid, intermolecular polar-π interactions originating from the alternating side chains influence the chain-folding process, thereby inducing the formation of a new type of superlattice based on conformational enantiomorphism.

All MD models were stable over 300 ns relaxation time and revealed similar trends in their lattice spacings (Figures S16–S19) with the values observed experimentally with PXRD and cryo-TEM analysis (Figure 2I), supporting the validity of the proposed molecular packing models for MD simulations. Figures 4B and 4C show the two molecules in a row extracted from relaxed nanosheets formed by homogeneous H_6 and F_6, respectively. The molecular arrangement remains stable in lattices. The relaxed packing of $(FH)_3$ molecules is shown in Figure 4E. The unique molecular packing with mirror-image backbones leads to an offset by one monomer along the *b*-axis, which remains stable after relaxation. In contrast to the racemic pairing of molecules in $(FH)_3$ nanosheets, the co-assembly of H_6 and F_6 molecules with the same backbone chirality directly enables perfluorophenyl-phenyl stacking without requiring an offset along the *b*-axis to form polar-π interactions (Figure 4F). DFT calculations on model tetramer peptoids revealed a strong driving force ($\approx$ 12 kcal/mol) for the alignment of phenylethyl and perfluorophenylethyl side chains along the *a*-axis, rather than homogeneous π-π interaction (Supplementary Note 3, Figure S20). These calculations clearly capture the relative energetic preference and electronic directionality favoring heteroaromatic (phenyl-

perfluorophenyl) alignment under backbone-imposed geometric constraints, qualitatively supporting polar-π interactions as a key electronic driving force for the observed alternating lattice registry. This registry enables the formation of the highly ordered superlattices observed in the $(FH)_3$ and co-assembled (H_6+F_6) nanosheets, as evidenced by the displaced sandwich stacking observed in relaxed MD models (Figure S21). [56, 57]

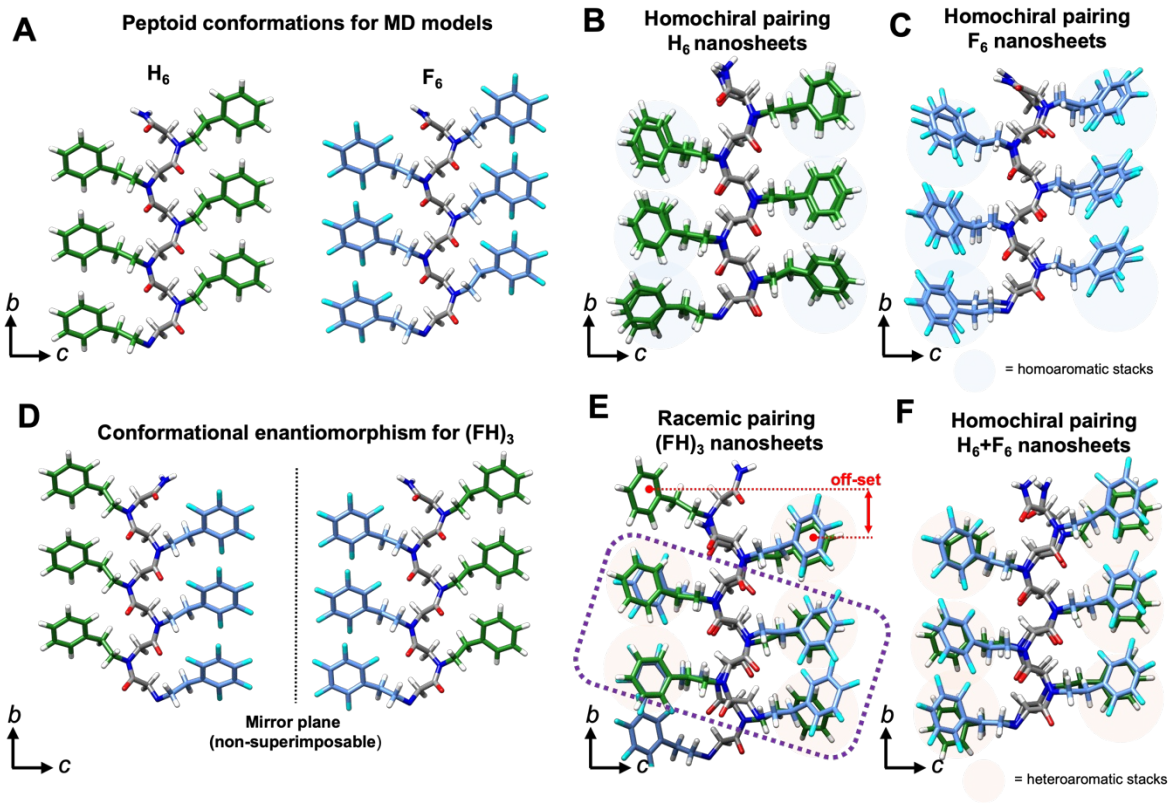

Figure 4. (A) Peptoid conformations used to build initial MD models of peptoid nanosheets assembled with H_6 or F_6. Maintained backbone pairings observed in relaxed MD models after 300 ns of (B) H_6 peptoid nanosheets (Figure S16) and (C) F_6 nanosheets (Figure S17). (D) Two peptoid conformation possessing opposite backbone chirality used to build initial MD models of $(FH)_3$ peptoid nanosheets. Backbone pairings observed in relaxed MD models after 300 ns of (E) $(FH)_3$ nanosheets (Figure S18) and (F) co-assembled H_6+F_6 nanosheets (Figure S19).

We further investigate the types and roles of noncovalent interactions that govern whether peptoid lattices adopt parallel or antiparallel orientations of molecules along the *c*-axis. DFT calculations were carried out based on the observation with the relaxed MD nanosheet models (Figures 5A and B). A parallel V-shaped packing motif shown in Figure 5A, formed by H_6 or F_6, in which the edge of side chains points to the center of another side chain along the *c*-axis, named the edge-to-center. In contrast, in an antiparallel V-shaped motif, formed by $(FH)_3$ or the 1:1 mixture of H_6 and F_6, as shown in Figure 5B, exhibit the side chains point linearly towards each other along the *c*-axis, named the edge-to-edge. The distinct side chain geometries indicate that small differences in aromatic polarization affect both the packing along the *a*-axis and the inter-row interactions that determine the motif along the *c*-axis.

DFT models were built to mimic side chain interactions in parallel and antiparallel V-shaped motifs. These models used aromatic fragments, specifically toluene (H) for phenylethyl side chains and pentafluorotoluene (F) for perfluorophenylethyl side chains. Edge-to-center inter-row interactions were constructed using four representative aromatic pairs: HH, FF, HF (with toluene positioned on top), and FH (with pentafluorotoluene positioned on top) (Figure 5C), while the edge-to-edge inter-row interactions are constructed using three representative aromatic pairs: FF, HF, and FH. (Figures 5D and S22).

In the edge-to-center geometry, homogenous HH and FF pairs exhibited stabilization at different van der Waals distances with varying energies. Heteroaromatic pairs (HF and FH) also showed distinct stabilization energies and van der Waals distances. The optimal van der Waals distance varies by approximately 0.5 Å depending on which aromatic ring is positioned on top (Figure 5C).

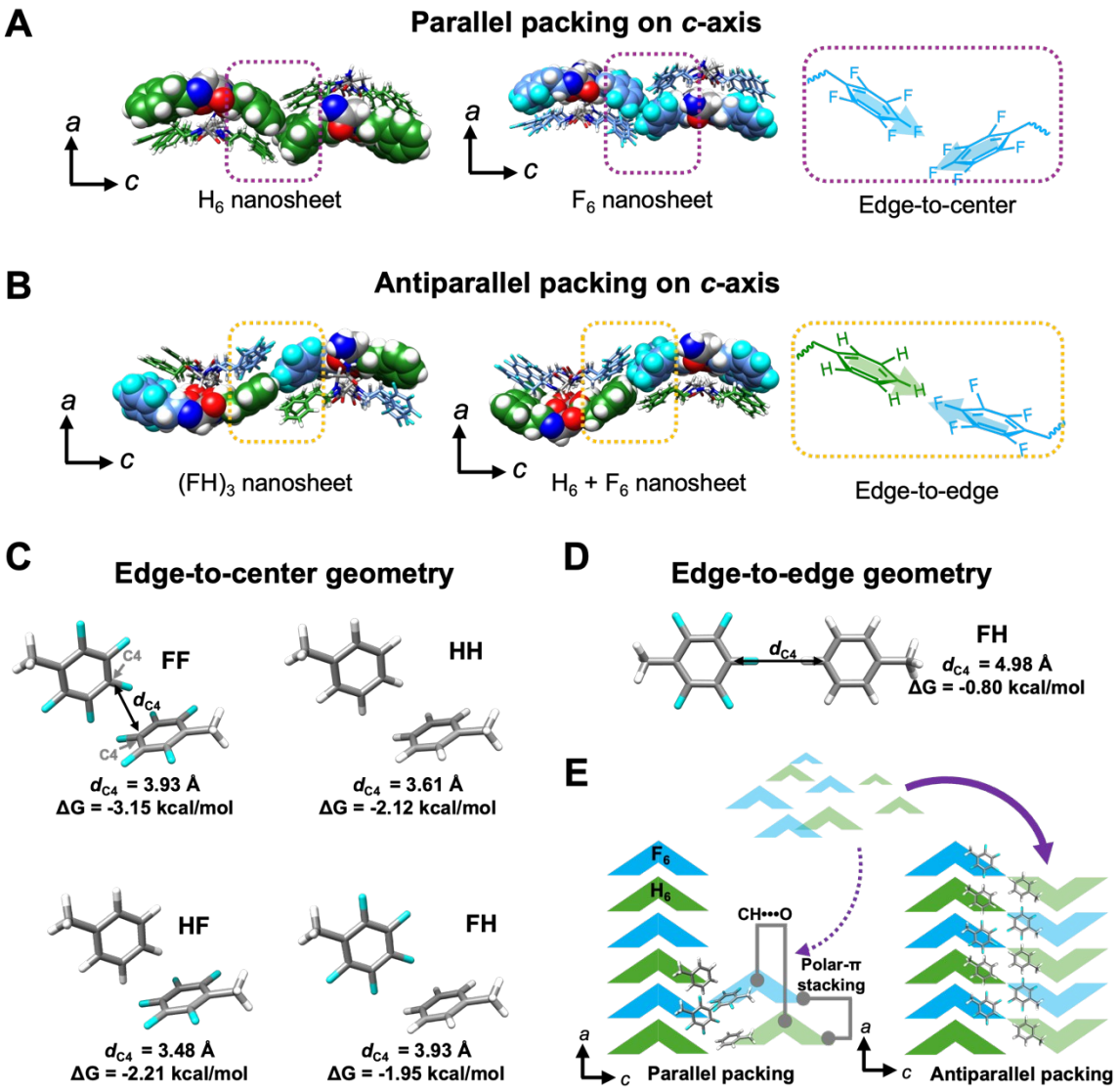

Figure 5. (A) Edge-to-center geometry observed in the *c*-direction in the relaxed MD models of H_6 nanosheets and F_6 nanosheets. (B) Edge-to-edge linear aromatic interactions observed in the *c*-direction in the relaxed MD models of $(FH)_3$ nanosheets and co-assembled H_6+F_6 nanosheets. (C) Representative geometry optimized models for the orthogonal edge-to-center geometry having homoaromatic interactions (FF and HH) and heteroaromatic interactions (HF and FH). 'F' indicates the model pentafluorotoluene mimicking perfluorophenylethyl side chains, and 'H' indicates the model toluene mimicking phenylethyl side chains. (D) Representative geometry optimized model for the linear edge-to-edge geometry having heteroaromatic

interaction (FH). (E) Schematic representation of the distortions in lattice with the parallel packing vs the antiparallel packing with H_6 (green chevrons) and F_6 (blue chevrons) peptoids.

The variable stabilization energies of the edge-to-center geometry can disrupt non-covalent interactions, such as CH•••O and polar-π interactions, in the parallel V-shaped packing motifs as shown in the schematic in Figure 5E (right panel). In contrast, edge-to-edge interactions in the antiparallel V-shaped packing motifs with heteroaromatic pairs (FH) are more stable and uniform, contributing to superlattice stability without disrupting other noncovalent interactions. The FH pair in edge-to-edge interactions prefers a shorter, more favorable interaction than homodimers (HH and FF) which further facilitate the formation of the regular lattice and superlattices (Supplementary Note 4. Figures S22A and S22B).

By integrating the experimentally determined crystal motifs and simulations, we obtained direct molecular level insight into how polar-π interactions modulate the formation of regular lattices with double spacing and binary superlattices with an antiparallel V-shape motif. Consequently, this work establishes a novel platform with well-defined binary lattices using the self-assembly of synthetic soft materials that remain free standing under aqueous conditions.

CONCLUSION

In this work, we demonstrated that the sequence-defined placement of electron-rich (*N*-2-phenylethyl) and electron-deficient (*N*-2-perfluorophenylethyl) aromatic side chains along a peptoid chain can be used to program polar-π interactions and thereby direct the formation of highly-ordered crystalline 2D nanosheets with either regular lattices or well-defined binary superlattices.

Cryo-TEM imaging at the atomic scale visualized the distinct arrangement of perfluorophenyl and phenyl rings, resulting in polar-π interactions that dominate the formation

of superlattices from those driven by π-π interactions. To our best knowledge, this is the first example where polar-π aromatic stacking in synthetic oligomeric lattices has been imaged in position space. Cryo-TEM imaging identified three distinct lattices in the crystalline nanosheets: the original all-phenyl lattice, a second lattice whose (100) *a* spacing is doubled relative to the original, and a binary superlattice that also displays a doubled (100) *a* spacing.

Diblock peptoids containing only perfluorophenylethyl side chains or only phenylethyl side chains formed regular lattices that adopt a parallel V-shaped crystal motif driven by π-π interactions. Diblock peptoids with alternating phenylethyl and perfluorophenylethyl side chains give rise to the regular lattice with the enlarged *a*-spacing, whereas the co-assembly of two complementary peptoid molecules, one bearing perfluorophenylethyl and the other phenylethyl side chains, leads to a highly stable binary superlattice with an antiparallel V-shaped motif that is stabilized by polar-π interactions, instead of a mixture of nanosheets composed of separated peptoid molecules. It suggests that polar-π interactions between the electron-deficient aromatic rings and the neutral aromatic rings drive the co-assembly into superlattices and enforces a highly ordered one-to-one (H_6+F_6) molecular alignment, exemplifying high-precision monolayer design at sub-nanometer scale, well beyond that have been observed within 2D superlattices comprising of synthetic soft materials.[24, 81-83]

While polar-π interactions provide specific recognition between phenyl and perfluorophenyl groups in small-molecule crystal engineering and host-guest systems,[84] translating this interaction into polymeric chain assemblies is highly nontrivial due to the complex conformational ensembles of chain molecules and entropy-driven phase separation,[85] which complicate the formation of homogeneous superlattices. For instance, block copolymers like polystyrene-*b*-polypentafluorostyrene, which carry aromatic side chains analogous to the phenyl and perfluorophenyl groups used in this study, are also known to exhibit pronounced

and exclusive phase separation due to differences in the solubility parameters of the side chains.[86, 87] To our knowledge, there are no reports of co-crystallization or melt miscibility in mixtures of fluorinated and nonfluorinated polymers. The results presented in this work suggest a new approach for realizing homogeneous binary crystalline materials based on fluorinated and nonfluorinated oligomeric systems that combine small-molecule-like atomic structural precision with polymer-like multidimensional conformational energy landscapes.

MD simulations and DFT calculations show that aromatic-polarization effects extend beyond simple facial stackings along the *a*-axis and edge-to-edge contacts along the *c*-axis that ultimately govern lattice stability and packing preferences in cooperation with backbone conformations. While fluorination alone does not disrupt lattice formation, enhanced thermal stability and unique lattice registry arise only when electronic complementarity is introduced into the system, as evidenced by comparative analysis of $(FH)_3$ and H_6+F_6 nanosheets. Together, these results disentangle polar-π interactions from steric effects and establish polar-π interactions as the dominant directional force controlling nanosheet packing and stability.

Our design principle leverages the robustness of peptoid unit cells, in which distinct noncovalent interactions are encoded along specific crystallographic axes, establishing a design logic for synthetic soft-matter superlattices where aromatic side-chain polarization and sequence govern unit cell alignment, lattice stability, and morphology. This strategy enables molecular-level precision in superlattice formation within ultrathin crystalline 2D soft materials in aqueous conditions and highlights the potential for extending this design logic to crystalline architectures of other dimensionalities (1D and 3D) under conditions where unit-cell registry is retained in soft crystalline materials.[55, 88] Direct visualization of polar-π interaction by cryo-TEM, coupled with atomistic modelling, provides a powerful framework for rationally

engineering monolayered 2D crystals with prescribed packing motifs using synthetic soft materials. The ability to precisely program binary superlattices opens new routes toward functional soft nanomaterials for selective molecular recognition and heterogeneous surface catalysis.

ACKNOWLEDGMENTS

This work was supported by the U.S. Department of Energy, Office of Science, Basic Energy Sciences, Materials Sciences and Engineering Division under Contract No. DE-AC02-05-CH11231 within the Soft Matter Electron Microscopy Program (KC11BN). Work at the Molecular Foundry at Lawrence Berkeley National Laboratory was supported by user projects at these user facilities, supported by the Office of Science, Office of Basic Energy Sciences, of the US Department of Energy under Contract DE-AC02-05CH11231. This research used resources of the Advanced Light Source, a U.S. DOE Office of Science User Facility under contract no. DE-AC02-05CH11231. Micrographs presented here were obtained at the Berkeley Bay Area Cryo-EM facility (BACEM) at the University of California, Berkeley. DFT calculations were carried out on the High Performance Computing resources at New York University Abu Dabi. We thank George Meigs, Mehagan Hopkins and James Holton for their assistance with the XRD measurements, Romas Kudirka, Natalia Molchanova and Michael Connolly for help with peptoid synthesis.

CONFLICT OF INTEREST

The authors declare no competing interest.

SUPPORTING INFORMATION

The Supporting Information includes materials synthesis, detailed experimental section, supplementary note 1-4, and supporting figures and tables (Figures S1-S22 and Tables S1 and S2) (PDF).

MD and DFT models are included:
PDB file showing the initial MD model of H_6 nanosheet (PDB)
PDB file showing the relaxed MD model of H_6 nanosheet (PDB)
PDB file showing the initial MD model of F_6 nanosheet (PDB)
PDB file showing the relaxed MD model of F_6 nanosheet (PDB)
PDB file showing the initial MD model of $(FH)_3$ nanosheet (PDB)
PDB file showing the relaxed MD model of $(FH)_3$ nanosheet (PDB)
PDB file showing the initial MD model of H_6+F_6 nanosheet (PDB)
PDB file showing the relaxed MD model of H_6+F_6 nanosheet (PDB)
PDB file showing the DFT geometry optimized structures of peptoid tetramer 1 and tetramer 2 mimicking heteroaromatic stack (PDB)
PDB file showing the DFT geometry optimized structures of two peptoid tetramer 1 mimicking homoaromatic stack (PDB)

REFERENCES

(1) Whitesides, G. M.; Mathias, J. P.; Seto, C. T. Molecular self-assembly and nanochemistry: a chemical strategy for the synthesis of nanostructures. *Science* **1991**, *254* (5036), 1312-1319. DOI: 10.1126/science.1962191.

(2) Alivisatos, A. P.; Barbara, P. F.; Castleman, A. W.; Chang, J.; Dixon, D. A.; Klein, M. L.; McLendon, G. L.; Miller, J. S.; Ratner, M. A.; Rossky, P. J.; et al. From molecules to materials: Current trends and future directions. *Adv. Mater.* **1998**, *10* (16), 1297-1336. DOI: 10.1002/(SICI)1521-4095(199811)10:16<1297::AID-ADMA1297>3.0.CO;2-7.

(3) Min, J.; Lee, H.; Park, M. J. Zwitterion-Stabilized Superlattices and Frank-Kasper Phases in Charged Block Copolymers for Mechanically Robust Dielectric Soft Materials. *Adv. Sci.* **2025**, *12* (36), e07115. DOI: 10.1002/advs.202507115.

(4) Peterson, D. A.; Farnsworth, T. W.; Woomer, A. H.; Fishman, Z. S.; Shapiro, S. H.; Radomsky, R. C.; Barron, E. A.; Thompson, J. R.; Warren, S. C. Generalized Assembly of Semiconductor–Molecule Superlattices. *Chem. Mat.* **2024**, *37* (1), 119-128. DOI: 10.1021/acs.chemmater.4c02165.

(5) Labastide, J. A.; Baghgar, M.; Dujovne, I.; Yang, Y.; Dinsmore, A. D.; G. Sumpter, B.; Venkataraman, D.; Barnes, M. D. Polymer Nanoparticle Superlattices for Organic Photovoltaic Applications. *J. Phys. Chem. Lett.* **2011**, *2* (24), 3085-3091. DOI: 10.1021/jz2012275.

(6) Dumele, O.; Chen, J.; Passarelli, J. V.; Stupp, S. I. Supramolecular Energy Materials. *Adv. Mater.* **2020**, *32* (17), e1907247. DOI: 10.1002/adma.201907247.

(7) Aida, T.; Meijer, E. W.; Stupp, S. I. Functional supramolecular polymers. *Science* **2012**, *335* (6070), 813-817. DOI: 10.1126/science.1205962.

(8) Uchida, M.; McCoy, K.; Fukuto, M.; Yang, L.; Yoshimura, H.; Miettinen, H. M.; LaFrance, B.; Patterson, D. P.; Schwarz, B.; Karty, J. A.; et al. Modular Self-Assembly of Protein Cage Lattices for Multistep Catalysis. *ACS Nano* **2018**, *12* (2), 942-953. DOI: 10.1021/acsnano.7b06049.

(9) Sun, L.; Yang, L.; Dou, J. H.; Li, J.; Skorupskii, G.; Mardini, M.; Tan, K. O.; Chen, T.; Sun, C.; Oppenheim, J. J.; et al. Room-Temperature Quantitative Quantum Sensing of Lithium Ions with a Radical-Embedded Metal-Organic Framework. *J. Am. Chem. Soc.* **2022**, *144* (41), 19008-19016. DOI: 10.1021/jacs.2c07692.

(10) Atzori, M.; Sessoli, R. The Second Quantum Revolution: Role and Challenges of Molecular Chemistry. *J. Am. Chem. Soc.* **2019**, *141* (29), 11339-11352. DOI: 10.1021/jacs.9b00984.

(11) Channon, K. J.; Devlin, G. L.; MacPhee, C. E. Efficient energy transfer within self-assembling peptide fibers: a route to light-harvesting nanomaterials. *J. Am. Chem. Soc.* **2009**, *131* (35), 12520-12521. DOI: 10.1021/ja902825j.

(12) Song, Q.; Goia, S.; Yang, J.; Hall, S. C. L.; Staniforth, M.; Stavros, V. G.; Perrier, S. Efficient Artificial Light-Harvesting System Based on Supramolecular Peptide Nanotubes in Water. *J. Am. Chem. Soc.* **2021**, *143* (1), 382-389. DOI: 10.1021/jacs.0c11060.

(13) Trinh, T. K. H.; Jin, B.; Zuckermann, R. N.; Chen, C. L. Assembly of Metalloporphyrin Peptoids into Crystalline Nanomaterials as a Multifunctional System for Biomimetic Catalysis and Sensing. *ACS Appl. Mater. Interfaces* **2025**, *17* (31), 44347-44359. DOI: 10.1021/acsami.5c05546.

(14) Jiang, J. H.; Zhao, S.; Sun, Y.; Wang, X. D. From Binary to Higher-Order Organic Cocrystals: Design Principles and Performance Optimization. *Angew. Chem. Int. Ed.* **2025**, *64* (28), e202507102. DOI: 10.1002/anie.202507102.

(15) Bhaumik, S.; Ntetsikas, K.; Hadjichristidis, N. Noncovalent Supramolecular Diblock Copolymers: Synthesis and Microphase Separation. *Macromolecules* **2020**, *53* (15), 6682-6689. DOI: 10.1021/acs.macromol.9b02326.

(16) Fleming, S.; Debnath, S.; Frederix, P. W.; Hunt, N. T.; Ulijn, R. V. Insights into the coassembly of hydrogelators and surfactants based on aromatic peptide amphiphiles. *Biomacromolecules* **2014**, *15* (4), 1171-1184. DOI: 10.1021/bm401720z.

(17) Ryan, D. M.; Doran, T. M.; Anderson, S. B.; Nilsson, B. L. Effect of C-terminal modification on the self-assembly and hydrogelation of fluorinated Fmoc-Phe derivatives. *Langmuir* **2011**, *27* (7), 4029-4039. DOI: 10.1021/la1048375.

(18) Halperin-Sternfeld, M.; Ghosh, M.; Sevostianov, R.; Grigoriants, I.; Adler-Abramovich, L. Molecular co-assembly as a strategy for synergistic improvement of the mechanical properties of hydrogels. *Chem. Commun.* **2017**, *53* (69), 9586-9589. DOI: 10.1039/c7cc04187j.

(19) Sinclair, J. C.; Davies, K. M.; Venien-Bryan, C.; Noble, M. E. Generation of protein lattices by fusing proteins with matching rotational symmetry. *Nat. Nanotechnol.* **2011**, *6* (9), 558-562. DOI: 10.1038/nnano.2011.122.

(20) Chou, T. F.; So, C.; White, B. R.; Carlson, J. C.; Sarikaya, M.; Wagner, C. R. Enzyme nanorings. *ACS Nano* **2008**, *2* (12), 2519-2525. DOI: 10.1021/nn800577h.

(21) Swanekamp, R. J.; DiMaio, J. T.; Bowerman, C. J.; Nilsson, B. L. Coassembly of enantiomeric amphipathic peptides into amyloid-inspired rippled beta-sheet fibrils. *J. Am. Chem. Soc.* **2012**, *134* (12), 5556-5559. DOI: 10.1021/ja301642c.

(22) Makam, P.; Gazit, E. Minimalistic peptide supramolecular co-assembly: expanding the conformational space for nanotechnology. *Chem. Soc. Rev.* **2018**, *47* (10), 3406-3420. DOI: 10.1039/c7cs00827a.

(23) Niece, K. L.; Hartgerink, J. D.; Donners, J. J.; Stupp, S. I. Self-assembly combining two bioactive peptide-amphiphile molecules into nanofibers by electrostatic attraction. *J. Am. Chem. Soc.* **2003**, *125* (24), 7146-7147. DOI: 10.1021/ja028215r.

(24) Ben-Sasson, A. J.; Watson, J. L.; Sheffler, W.; Johnson, M. C.; Bittleston, A.; Somasundaram, L.; Decarreau, J.; Jiao, F.; Chen, J.; Mela, I.; et al. Design of biologically active binary protein 2D materials. *Nature* **2021**, *589* (7842), 468-473. DOI: 10.1038/s41586-020-03120-8.

(25) Li, X.; Qiao, S.; Zhao, L.; Liu, S.; Li, F.; Yang, F.; Luo, Q.; Hou, C.; Xu, J.; Liu, J. Template-Free Construction of Highly Ordered Monolayered Fluorescent Protein Nanosheets: A Bioinspired Artificial Light-Harvesting System. *ACS Nano* **2019**, *13* (2), 1861-1869. DOI: 10.1021/acsnano.8b08021.

(26) Hsu, S.-W.; Xu, T. Tailoring Co-assembly of Nanodiscs and Block Copolymer-Based Supramolecules by Manipulating Interparticle Interactions. *Macromolecules* **2019**, *52* (7), 2833-2842. DOI: 10.1021/acs.macromol.9b00069.

(27) Liu, L.; Meng, X.; Li, M.; Chu, Z.; Tong, Z. Regulation of Two-Dimensional Platelet Micelles with Tunable Core Composition Distribution via Coassembly Seeded Growth Approach. *ACS Macro. Lett.* **2024**, *13* (5), 542-549. DOI: 10.1021/acsmacrolett.4c00124.

(28) Xu, T.; Zhao, N.; Ren, F.; Hourani, R.; Lee, M. T.; Shu, J. Y.; Mao, S.; Helms, B. A. Subnanometer porous thin films by the co-assembly of nanotube subunits and block copolymers. *ACS Nano* **2011**, *5* (2), 1376-1384. DOI: 10.1021/nn103083t.

(29) Macfarlane, R. J.; Lee, B.; Jones, M. R.; Harris, N.; Schatz, G. C.; Mirkin, C. A. Nanoparticle superlattice engineering with DNA. *Science* **2011**, *334* (6053), 204-208. DOI: 10.1126/science.1210493.

(30) Qi, X.; Helland, S.; Lowe, C. D.; Larson, H.; Cui, J.; Zheng, R.; Monahan, M.; Chen, C. L.; De Yoreo, J.; Pfaendtner, J.; et al. Toward Computation-Guided Design of Tunable Organic-Inorganic CdS Quantum Dot Binary Superlattices. *Nano Lett.* **2025**, *25* (10), 3989-3996. DOI: 10.1021/acs.nanolett.5c00024.

(31) Safont-Sempere, M. M.; Fernandez, G.; Wurthner, F. Self-sorting phenomena in complex supramolecular systems. *Chem. Rev.* **2011**, *111* (9), 5784-5814. DOI: 10.1021/cr100357h.

(32) Wu, A.; Isaacs, L. Self-sorting: the exception or the rule? *J. Am. Chem. Soc.* **2003**, *125* (16), 4831-4835. DOI: 10.1021/ja028913b.

(33) Kitamoto, Y.; Pan, Z.; Prabhu, D. D.; Isobe, A.; Ohba, T.; Shimizu, N.; Takagi, H.; Haruki, R.; Adachi, S. I.; Yagai, S. One-shot preparation of topologically chimeric nanofibers via a gradient supramolecular copolymerization. *Nat. Commun.* **2019**, *10* (1), 4578. DOI: 10.1038/s41467-019-12654-z.

(34) Matsumoto, K.; Baumer, N.; Ogi, S.; Yamaguchi, S. Kinetic Control over Social and Narcissistic Self-Sorting from Multicomponent Mixtures in Seed-Initiated Supramolecular Polymerization by Fine-Tuning of Steric Effects. *Angew. Chem. Int. Ed.* **2025**, *64* (4), e202416361. DOI: 10.1002/anie.202416361.

(35) Wen, X.; Jiang, H.; Wang, R.; Zhang, L.; Liu, M. Photo-Decrypted Narcissistic Self-Sorting in Chirality-Driven Supramolecular System. *Angew. Chem. Int. Ed.* **2025**, *64* (39), e202510748. DOI: 10.1002/anie.202510748.

(36) Matsen, M. W.; Bates, F. S. Unifying weak- and strong-segregation block copolymer theories. *Macromolecules* **1996**, *29* (4), 1091-1098. DOI: DOI 10.1021/ma951138i.

(37) Heiber, M. C.; Baumbach, C.; Dyakonov, V.; Deibel, C. Encounter-limited charge-carrier recombination in phase-separated organic semiconductor blends. *Phys. Rev. Lett.* **2015**, *114* (13), 136602. DOI: 10.1103/PhysRevLett.114.136602.

(38) Zuckermann, R. N.; Kerr, J. M.; Kent, S. B. H.; Moos, W. H. Efficient Method for the Preparation of Peptoids [Oligo(N-Substituted Glycines)] by Submonomer Solid-Phase Synthesis. *J. Am. Chem. Soc.* **1992**, *114* (26), 10646-10647. DOI: 10.1021/ja00052a076.

(39) Kang, L.; Chao, A.; Zhang, M.; Yu, T.; Wang, J.; Wang, Q.; Yu, H.; Jiang, N.; Zhang, D. Modulating the Molecular Geometry and Solution Self-Assembly of Amphiphilic Polypeptoid Block Copolymers by Side Chain Branching Pattern. *J. Am. Chem. Soc.* **2021**, *143* (15), 5890-5902. DOI: 10.1021/jacs.1c01088.

(40) Ding, X.; Liu, D.; Jiang, X.; Chen, X.; Zuckermann, R. N.; Sun, J. Hierarchical Approach for Controlled Assembly of Branched Nanostructures from One Polymer Compound by Engineering Crystalline Domains. *ACS Nano* **2022**, *16* (7), 10470-10481. DOI: 10.1021/acsnano.2c01171.

(41) Jin, H.; Jiao, F.; Daily, M. D.; Chen, Y.; Yan, F.; Ding, Y. H.; Zhang, X.; Robertson, E. J.; Baer, M. D.; Chen, C. L. Highly stable and self-repairing membrane-mimetic 2D nanomaterials assembled from lipid-like peptoids. *Nat. Commun.* **2016**, *7*, 12252. DOI: 10.1038/ncomms12252.

(42) Xuan, S.; Jiang, X.; Spencer, R. K.; Li, N. K.; Prendergast, D.; Balsara, N. P.; Zuckermann, R. N. Atomic-level engineering and imaging of polypeptoid crystal lattices. *Proc. Natl. Acad. Sci. U. S. A.* **2019**, *116* (45), 22491-22499. DOI: 10.1073/pnas.1909992116.

(43) Trinh, T. K. H.; Jian, T.; Jin, B.; Nguyen, D. T.; Zuckermann, R. N.; Chen, C. L. Designed Metal-Containing Peptoid Membranes as Enzyme Mimetics for Catalytic Organophosphate Degradation. *ACS Appl. Mater. Interfaces* **2023**, *15* (44), 51191-51203. DOI: 10.1021/acsami.3c11816.

(44) Chakma, P.; Chen, Y.; Harris, B. S.; Elhady, Y. W.; Zheng, R.; Bowden, M. E.; Shutthanandan, V.; Bard, A. B.; Trinh, T. K. H.; Zheng, X.; et al. Assembled peptoid crystalline nanomaterials as carbonic anhydrase mimics for promoted hydration and sequestration of CO(2). *Nat. Commun.* **2025**, *16* (1), 7348. DOI: 10.1038/s41467-025-62366-w.

(45) Yu, T.; Luo, X.; Prendergast, D.; Butterfoss, G. L.; Rad, B.; Balsara, N. P.; Zuckermann, R. N.; Jiang, X. Structural Elucidation of a Polypeptoid Chain in a Crystalline Lattice

Reveals Key Morphology-Directing Role of the N-Terminus. *ACS Nano* **2023**, *17* (5), 4958-4970. DOI: 10.1021/acsnano.2c12503.

(46) Seidler, M.; Li, N. K.; Luo, X.; Xuan, S.; Zuckermann, R. N.; Balsara, N. P.; Prendergast, D.; Jiang, X. Importance of the Positively Charged sigma-Hole in Crystal Engineering of Halogenated Polypeptoids. *J Phys Chem B* **2022**, *126* (22), 4152-4159. DOI: 10.1021/acs.jpcb.2c01843.

(47) Jiang, X.; Seidler, M.; Butterfoss, G. L.; Luo, X.; Yu, T.; Xuan, S.; Prendergast, D.; Zuckermann, R. N.; Balsara, N. P. Atomic-Scale Corrugations in Crystalline Polypeptoid Nanosheets Revealed by Three-Dimensional Cryogenic Electron Microscopy. *ACS Macro Lett.* **2023**, *12* (5), 632-638. DOI: 10.1021/acsmacrolett.3c00101.

(48) Nam, K. T.; Shelby, S. A.; Choi, P. H.; Marciel, A. B.; Chen, R.; Tan, L.; Chu, T. K.; Mesch, R. A.; Lee, B. C.; Connolly, M. D.; et al. Free-floating ultrathin two-dimensional crystals from sequence-specific peptoid polymers. *Nat. Mater.* **2010**, *9* (5), 454-460. DOI: 10.1038/nmat2742.

(49) Rich-New, S. T.; Wang, R.; Zia, A.; Wang, F.; Tovar, J. D. Cryo-EM Visualization of Intermolecular pi-Electron Interactions within pi-Conjugated Peptidic Supramolecular Polymers. *ACS Macro. Lett.* **2025**, *14* (8), 1100-1106. DOI: 10.1021/acsmacrolett.5c00360.

(50) Bigo-Simon, A.; Estrozi, L. F.; Chaumont, A.; Schurhammer, R.; Schoehn, G.; Combet, J.; Schmutz, M.; Schaaf, P.; Jierry, L. 3D Cryo-Electron Microscopy Reveals the Structure of a 3-Fluorenylmethyloxycarbonyl Zipper Motif Ensuring the Self-Assembly of Tripeptide Nanofibers. *Acs Nano* **2024**, *18* (44), 30448-30462. DOI: 10.1021/acsnano.4c08043.

(51) Sonani, R. R.; Bianco, S.; Kreutzberger, M. A. B.; Adams, D. J.; Egelman, E. H. Cryo-EM for atomic characterization of supramolecular gels. *Faraday Discuss* **2025**, *260* (0), 132-144. DOI: 10.1039/d4fd00181h.

(52) Wang, F.; Gnewou, O.; Solemanifar, A.; Conticello, V. P.; Egelman, E. H. Cryo-EM of Helical Polymers. *Chem. Rev.* **2022**, *122* (17), 14055-14065. DOI: 10.1021/acs.chemrev.1c00753.

(53) Solinc, G.; Srnko, M.; Merzel, F.; Crnkovic, A.; Kozorog, M.; Podobnik, M.; Anderluh, G. Cryo-EM structures of a protein pore reveal a cluster of cholesterol molecules and diverse roles of membrane lipids. *Nat. Commun.* **2025**, *16* (1), 2972. DOI: 10.1038/s41467-025-58334-z.

(54) Gallagher-Jones, M.; Glynn, C.; Boyer, D. R.; Martynowycz, M. W.; Hernandez, E.; Miao, J.; Zee, C. T.; Novikova, I. V.; Goldschmidt, L.; McFarlane, H. T.; et al. Sub-angstrom cryo-EM structure of a prion protofibril reveals a polar clasp. *Nat. Struct. Mol. Biol.* **2018**, *25* (2), 131-134. DOI: 10.1038/s41594-017-0018-0.

(55) Lee, Y. J.; Seidler, M.; Luo, X.; Butterfoss, G. L.; Yu, T.; Rad, B.; Xuan, S.; Zhu, C.; Prendergast, D.; Balsara, N. P.; et al. Crystalline Peptoid Nanofibers with a Single-Unit Cell Cross Section. *J. Am. Chem. Soc.* **2025**, *147* (31), 27390-27402. DOI: 10.1021/jacs.5c03996.

(56) Gung, B. W.; Xue, X.; Zou, Y. Enthalpy (DeltaH) and entropy (DeltaS) for pi-stacking interactions in near-sandwich configurations: relative importance of electrostatic, dispersive, and charge-transfer effects. *J. Org. Chem.* **2007**, *72* (7), 2469-2475. DOI: 10.1021/jo062526t.

(57) Tsuzuki, S.; Uchimaru, T.; Mikami, M. Intermolecular interaction between hexafluorobenzene and benzene: Ab initio calculations including CCSD(T) level electron correlation correction. *J. Phys. Chem. A* **2006**, *110* (5), 2027-2033. DOI: 10.1021/jp054461o.

(58) Hunter, C. A.; Sanders, J. K. M. The nature of .pi.-.pi. interactions. *J. Am. Chem. Soc.* **2002**, *112* (14), 5525-5534. DOI: 10.1021/ja00170a016.

(59) Cozzi, F.; Cinquini, M.; Annunziata, R.; Dwyer, T.; Siegel, J. S. Polar/Pi Interactions between Stacked Aryls in 1,8-Diarylnaphthalenes. *J. Am. Chem. Soc.* **1992**, *114* (14), 5729-5733. DOI: DOI 10.1021/ja00040a036.

(60) Nguyen, A. I.; Ganatra, P.; Hess, S. S.; Nichols, S.; Heinz-Kunert, S. L. Advances in the design of π-conjugated peptide assemblies. *Trends in Chemistry* **2025**, *7* (5), 225-239. DOI: 10.1016/j.trechm.2025.03.002.

(61) Weck, M.; Dunn, A. R.; Matsumoto, K.; Coates, G. W.; Lobkovsky, E. B.; Grubbs, R. H. Influence of Perfluoroarene-Arene Interactions on the Phase Behavior of Liquid Crystalline and Polymeric Materials. *Angew. Chem. Int. Ed.* **1999**, *38* (18), 2741-2745. DOI: 10.1002/(sici)1521-3773(19990917)38:18<2741::Aid-anie2741>3.0.Co;2-1.

(62) Hu, J.; He, C.; Zheng, X.; Li, Y.; Yang, X.; Wang, W.; Zhang, J.; Chen, Q.; Huang, F.; Fu, W.; et al. Tailoring Self-Assembled Monolayers for High-Performance Polymer Solar Cells with Improved Stability. *Solar RRL* **2023**, *7* (6), 2201106. DOI: 10.1002/solr.202201106.

(63) Hope, M. A.; Nakamura, T.; Ahlawat, P.; Mishra, A.; Cordova, M.; Jahanbakhshi, F.; Mladenovic, M.; Runjhun, R.; Merten, L.; Hinderhofer, A.; et al. Nanoscale Phase Segregation in Supramolecular pi-Templating for Hybrid Perovskite Photovoltaics from NMR Crystallography. *J. Am. Chem. Soc.* **2021**, *143* (3), 1529-1538. DOI: 10.1021/jacs.0c11563.

(64) Kim, T.; Hong, J.; Kim, J.; Cho, J.; Kim, Y. Two-Dimensional Peptide Assembly via Arene-Perfluoroarene Interactions for Proliferation and Differentiation of Myoblasts. *J. Am. Chem. Soc.* **2023**, *145* (3), 1793-1802. DOI: 10.1021/jacs.2c10938.

(65) Zhang, S.; Chen, A.; An, Y.; Li, Q. Arene-perfluoroarene interaction: Properties, constructions, and applications in materials science. *Matter* **2024**, *7* (10), 3317-3350. DOI: 10.1016/j.matt.2024.06.035.

(66) Collings, J. C.; Roscoe, K. P.; Thomas, R. L.; Batsanov, A. S.; Stimson, L. M.; Howard, J. A. K.; Marder, T. B. Arene-perfluoroarene interactions in crystal engineering. Part 3. Single-crystal structures of 1 : 1 complexes of octafluoronaphthalene with fused-ring polyaromatic hydrocarbons. *New J. Chem.* **2001**, *25* (11), 1410-1417. DOI: 10.1039/b105502j.

(67) Patrick, C. R.; Prosser, G. S. A Molecular Complex of Benzene and Hexafluorobenzene. *Nature* **1960**, *187* (4742), 1021-1021. DOI: 10.1038/1871021a0.

(68) Williams, J. H.; Cockcroft, J. K.; Fitch, A. N. Structure of the Lowest Temperature Phase of the Solid Benzene–Hexafluorobenzene Adduct. *Angewandte Chemie International Edition in English* **1992**, *31* (12), 1655-1657. DOI: 10.1002/anie.199216551.

(69) Reichenbacher, K.; Suss, H. I.; Hulliger, J. Fluorine in crystal engineering—"the little atom that could". *Chem. Soc. Rev.* **2005**, *34* (1), 22-30. DOI: 10.1039/b406892k.

(70) Hsu, S. M.; Lin, Y. C.; Chang, J. W.; Liu, Y. H.; Lin, H. C. Intramolecular interactions of a phenyl/perfluorophenyl pair in the formation of supramolecular nanofibers and hydrogels. *Angew. Chem. Int. Ed.* **2014**, *53* (7), 1921-1927. DOI: 10.1002/anie.201307500.

(71) Zhang, H.; Lou, S.; Yu, Z. Polar-pi Interactions Promote Self-assembly of Dipeptides into Laminated Nanofibers. *Langmuir* **2019**, *35* (13), 4710-4717. DOI: 10.1021/acs.langmuir.9b00077.

(72) Cheng, Q.; Hao, A.; Xing, P. Selective chiral dimerization and folding driven by arene-perfluoroarene force. *Chem. Sci.* **2024**, *15* (2), 618-628. DOI: 10.1039/d3sc05212e.

(73) Roesner, E. K.; Asheghali, D.; Kirillova, A.; Strauss, M. J.; Evans, A. M.; Becker, M. L.; Dichtel, W. R. Arene-perfluoroarene interactions confer enhanced mechanical properties to synthetic nanotubes. *Chem. Sci.* **2022**, *13* (8), 2475-2480. DOI: 10.1039/d1sc05932g.

(74) Tanaka, M.; Takigawa, H.; Yasaka, Y.; Shono, T.; Funazo, K.; Wu, H.-L. Derivatization of inorganic anions with pentafluorobenzyl methanesulphonate for gas chromatography. *J. Chromatogr. A* **1987**, *404*, 175-182. DOI: 10.1016/s0021-9673(01)86848-5.

(75) Giese, M.; Albrecht, M.; Wiemer, K.; Valkonen, A.; Rissanen, K. Controlling the position of anions relative to a pentafluorophenyl group. *New J. Chem.* **2012**, *36* (6) 1368-1372. DOI: 10.1039/c2nj40089h.

(76) Greer, D. R.; Stolberg, M. A.; Kundu, J.; Spencer, R. K.; Pascal, T.; Prendergast, D.; Balsara, N. P.; Zuckermann, R. N. Universal Relationship between Molecular Structure and Crystal Structure in Peptoid Polymers and Prevalence of the cis Backbone Conformation. *J. Am. Chem. Soc.* **2018**, *140* (2), 827-833. DOI: 10.1021/jacs.7b11891.

(77) Hudson, B. C.; Battigelli, A.; Connolly, M. D.; Edison, J.; Spencer, R. K.; Whitelam, S.; Zuckermann, R. N.; Paravastu, A. K. Evidence for cis Amide Bonds in Peptoid Nanosheets. *J. Phys. Chem. Lett.* **2018**, *9* (10), 2574-2578. DOI: 10.1021/acs.jpclett.8b01040.

(78) Edison, J. R.; Spencer, R. K.; Butterfoss, G. L.; Hudson, B. C.; Hochbaum, A. I.; Paravastu, A. K.; Zuckermann, R. N.; Whitelam, S. Conformations of peptoids in nanosheets result from the interplay of backbone energetics and intermolecular interactions. *Proc. Natl. Acad. Sci. U. S. A.* **2018**, *115* (22), 5647-5651. DOI: 10.1073/pnas.1800397115.

(79) Spencer, R. K.; Butterfoss, G. L.; Edison, J. R.; Eastwood, J. R.; Whitelam, S.; Kirshenbaum, K.; Zuckermann, R. N. Stereochemistry of polypeptoid chain configurations. *Biopolymers* **2019**, *110* (6), e23266. DOI: 10.1002/bip.23266.

(80) Mannige, R. V.; Haxton, T. K.; Proulx, C.; Robertson, E. J.; Battigelli, A.; Butterfoss, G. L.; Zuckermann, R. N.; Whitelam, S. Peptoid nanosheets exhibit a new secondary-structure motif. *Nature* **2015**, *526* (7573), 415-420. DOI: 10.1038/nature15363.

(81) Chen, L.; Lee, H. S.; Lee, S. Close-packed block copolymer micelles induced by temperature quenching. *Proc. Natl. Acad. Sci. U. S. A.* **2018**, *115* (28), 7218-7223. DOI: 10.1073/pnas.1801682115.

(82) Chen, H.; Liu, Y.; Zhang, T.; Zhao, G. Construction of three-dimensional interleaved protein hetero-superlattices in solution by cooperative electrostatic and aromatic stacking interactions. *J. Colloid Interface Sci.* **2021**, *582* (Pt A), 1-11. DOI: 10.1016/j.jcis.2020.08.016.

(83) Abbas, S.; Lodge, T. P. Superlattice formation in binary mixtures of block copolymer micelles. *Langmuir* **2008**, *24* (12), 6247-6253. DOI: 10.1021/la8002367.

(84) Huang, Z.; Chen, X.; Wu, G.; Metrangolo, P.; Whitaker, D.; McCune, J. A.; Scherman, O. A. Host-Enhanced Phenyl-Perfluorophenyl Polar-pi Interactions. *J. Am. Chem. Soc.* **2020**, *142* (16), 7356-7361. DOI: 10.1021/jacs.0c02275.

(85) Scott, R. L.; Magat, M. The Thermodynamics of High-Polymer Solutions: I. The Free Energy of Mixing of Solvents and Polymers of Heterogeneous Distribution. *J. Chem. Phys.* **1945**, *13* (5), 172-177. DOI: 10.1063/1.1724018.

(86) Mandal, P.; Marcasuzaa, P.; Billon, L. para-Fluoro/thiol click chemistry-driven pentafluorostyrene-based block copolymer self-assembly: to mimic or not to mimic the solubility parameter? *Polym. Chem.* **2022**, *13* (33), 4757-4762. DOI: 10.1039/d2py00784c.

(87) Semsarilar, M.; Greenall, M. J.; Balzer, A. H.; Sarkar, A. K.; Gomri, C.; Benkhaled, B. T.; Höhme, A.-L.; Held, M.; Abetz, V.; Hutchins-Crawford, H. J.; et al. Exploring Microphase Separation in Semi-Fluorinated Diblock Copolymers: A Combined Experimental and Modeling Investigation. *ACS Polymers Au* **2025**. DOI: 10.1021/acspolymersau.5c00109.

(88) Lee, Y. J.; Ercius, P.; Luo, X.; Butterfoss, G. L.; Yu, T.; Zhang, J.; Prendergast, D.; Minor, A. M.; Balsara, N. P.; Zuckermann, R. N.; et al. Three-Dimensional Crystals Assembled by Linear Oligopeptoids. *Nano Lett.* **2025**, *25* (31), 11940-11946. DOI: 10.1021/acs.nanolett.5c02506.

Table of Content